Journal of Ultrafine Grained and Nanostructured Materials
https://jufgnsm.ut.ac.ir
Vol. 55, No.1, June 2022, pp. 1-9
Print ISSN: 2423-6845 Online ISSN: 2423-6837
DOI: 10.22059/jufgnsm.2022.01.01

Effect of coating frequency on the corrosion performance of PEO coatings on AZ31B Mg alloy produced in an electrolyte containing hydroxyapatite nanoparticles

Razieh Chaharmahali, Arash Fattah-alhosseini*

Department of Materials Engineering, Bu-Ali Sina University, Hamedan 65178-38695, Iran.

Recieved: 11 October 2021; Accepted: 12 January 2022

**Corresponding author email: a.fattah@basu.ac.ir*

ABSTRACT

In this study, to improve the corrosion performance, plasma electrolytic oxidation (PEO) coatings on AZ31B Mg alloy in a phosphate-based electrolyte containing hydroxyapatite nanoparticles were investigated. For this purpose, the corrosion behavior of coatings generated at different frequencies (100, 1000, and 2000 Hz) was studied. The influence of coating frequency on the corrosion behavior of the coatings created as well as the microstructure of the coating was investigated. Surface characteristics of the coatings were investigated using scanning electron microscopy and X-ray diffraction pattern. To investigate the corrosion behavior of coatings generated at different frequencies, polarization and impedance spectroscopy tests in simulated body fluid have been studied. The results showed that at a frequency of 1000 Hz, the created coating had a uniform surface with a lower porosity percentage. Also, the results of electrochemical tests showed that the corrosion resistance of the coating created at a frequency of 1000 Hz leads to the lowest corrosion current density (5.83×10^{-8} A/cm^2) in the coating and thus more became the most corrosion resistant.

Keywords: *AZ31B Mg alloy; Plasma electrolytic oxidation (PEO); Corrosion behavior; simulated body fluid (SBF); frequency.*

1. Introduction

The lightest metal among of all the engineering metals is magnesium with a density of 1.7 g/cm^3. Its most important advantages are high strength to weight ratio, good casting capability in controlled conditions, and machining capability, which has expanded its application in various industries such as electronics, aerospace, and transportation [1]–[5]. Mg and its alloys are one of the most important and widely used biodegradable materials that are used in various medical applications. Mg is known as a biologically suitable material due to its good biocompatibility and biodegradability properties as well as desirable mechanical properties. The Young modulus and density of magnesium and its alloys are very similar to bone compared to other implants, which reduces the stress in the joint between bone and implant and increases bone growth and implant stability [6]–[10]. However, the main problem with Mg and its alloys is the high corrosion rate in the body, which limits their use. The low corrosion performance of magnesium and its alloys leads to reduced mechanical stability and undesirable appearance [11]–[16].

To improve the use of magnesium and its alloys as implants, the amount of corrosion and its destruction in the body environment must be controlled. Various coating methods have been studied to protect Mg and its alloys against corrosion, including sol-gel methods [17], chemical vapor deposition [18], and plasma electrolytic oxidation (PEO) [19]–[25]. Among the mentioned

methods, the PEO method is a new surface process for creating ceramic coatings on metals such as Al, Mg, Ti, Zr, and Nb [26]–[32]. The coating created by this process improves the corrosion and abrasion behavior of the metal and can increase the biocompatibility of the metal by creating hydroxyapatite coatings [33]. This method typically involves immersing a metal base in an alkaline electrolyte. The advantages of coatings created in this way include high hardness, good adhesion between the substrate and the coating, simplicity of equipment and no need for vacuum and gas protection conditions, and the possibility of coating parts with complex and large shapes [34]–[39].

Numerous factors such as substrate, electrolyte, time, temperature, additive and electrical parameters such as voltage, frequency, duty cycle, and current density affect the properties of the coating created by the PEO process [40]–[50]. Among these, electrical parameters have a great impact on the quality and properties of the coating. Among the electrical parameters, researchers have inferred that the applied frequency, which makes sense in the type of pulse applied current, has a significant effect on the microstructure of the coating by affecting ignition voltage [51]. Since the applied frequency controls the rate of disconnection and connection of the circuit between the anode and the cathode, it can control the time of establishment and connection of the current and as a result it can cause the disconnection of individual micro-sparks at high frequencies [47], [51]–[54]. In this study, the effect of different frequencies (100, 1000, and 2000 Hz) in coatings containing hydroxyapatite nanoparticles on magnesium alloy, which caused significant changes in the microstructure and porosity of the coating, and then the corrosion behavior of coatings tested in simulated body fluid (SBF).

2. Experimental Process

2.1. PEO process

In the coating process, the sheet of AZ31B alloy was used as metallic substrates [55]. To perform the coating process, the samples were cut into rectangular cubes with dimensions of $20 \times 15 \times 3$ mm^3 by a cutting machine. Before the coating process, all samples were sanded with SiC sandpapers numbers 220, 400, 600, 800, and 1000, respectively, and then washed with distilled water and blown with cold air. The electrolyte used in this process was a combination of 5 g/L $Na_3PO_4.12H_2O$, 3 g/L KOH, and 15 g/L hydroxy apatite nanoparticles. Synthesis of hydroxyapatite nanoparticles used in this research was carried out using the wet chemical precipitation method. Particles are typically quasi-spherical in shape, and their size is estimated to be 165 nanometers. The previous study [55] detailed the steps involved in creating hydroxyapatite nanoparticles as well as the outcomes. Power supply model PM 700/7 PRC was used to perform the coating process. The conditions for coating samples at different frequencies are specified in Table 1.

2.2. Surface characterization and corrosion measurements

Surface characteristics of coatings were studied using scanning electron microscopy (SEM), and X-ray diffraction (XRD). A detailed description of the SEM and XRD tests can be found in a previous publication [55]. Potentiodynamic polarization (PDP) and electrochemical impedance spectroscopy (EIS) tests were performed on uncoated and coated AZ31B alloy in SBF solution. The corrosion tests were carried out using three-electrode flat cells. As an auxiliary electrode, a Pt electrode was employed, together with an Ag/AgCl reference electrode and the examined sample as a working electrode. EIS testing was performed on all specimens with a frequency range of 100 kHz to 10 mHz. Before any test, the samples were placed in SBF solution for 1800 s to reach a steady-state under open circuit potential conditions. The SBF was prepared based on the Kokubo method. A detailed description of the EIS and PDP tests can be found in a previous publication [55].

3. Results and Discussion

3.1. Voltage-time diagram

Properties of coating generated by PEO method

Table 1- Chemical composition of the used electrolyte in the coating

Sample	Frequency (Hz)	Duty cycle (%)	Time (min)	Current density (A)
f 100	100	50	7	1
f 1000	1000	50	7	1
f 2000	2000	50	7	1

under the influence of voltage characteristics such as final voltage, and breakdown voltage. For example, the breakdown voltage indicates the tendency metal is the primary barrier layer formation. The final voltage indicates the tendency of the metal to achieve a stable resistance of the layer. Therefore, the study of voltage changes in terms of oxidation time can be used to better understand the properties of the coating. Fig. 1 shows the effect of frequency (100, 1000, and 2000 Hz) on the voltage-time plot during PEO operation.

The values of critical voltage, breakdown voltage, and final voltage for the samples are given in Table 2. As shown in Fig. 1, the voltage-time plot of the PEO process is divided into three stages, which is also consistent with the plasma physics perspective of this type of process. The first step (I) is the anodic oxidation region and covers from the beginning of the process to the breakdown voltage. At this stage, the voltage increases rapidly and linearly, which indicates the formation of an insulating and thin oxide layer on the substrate surface. The second stage (II) is the area of micro-spark oxidation and includes from the breakdown voltage to the critical voltage, this stage begins with the ignition process. The relationship between voltage fluctuations and time is nonlinear, with tiny white sparks moving rapidly over the surface of the sample, covering the entire surface. The third stage (III) is called the stable micro-spark oxidation zone. At this stage, the voltage increases with a slight slope relative to the critical voltage and its changes are fixed over time and continue until the final voltage [45], [56]–[60].

The results show that changing the frequency from 100 to 2000 Hz leads to a change in ignition voltage and final voltage. It can be said that the life of sparks depends on the frequency. Based on the voltage-time curve, it can be said that as the frequency decreases, the amount of ignition voltage increases. The mechanism of the process is such that by reducing the frequency due to the longer life and power of the sparks, the process needs more voltages. Also, at higher frequencies, the spark life is shorter (less energy) and the process requires less voltage to start ignition. Then, with decreasing frequency, the final voltage has increased, which in the final stage of coating growth will lead to the creation of extremely strong arcs on the surface of the coating.

Table 2- Results extracted from voltage-time diagram

Sample	Breakdown voltage (V)	Final voltage (V)
f100	367	650
f 1000	325	620
f 2000	300	570

3.2. Characterization of the coating surface

SEM images of coated specimens at different frequencies (100, 1000, and 2000) are shown in Fig. 2. As can be seen, due to the formation of sparks during the coating process, all coatings have a porous surface and cracks are formed due to the release of thermal stresses during the coating process [61]–[65].

The percentage of porosity is shown in Fig. 3. It can be seen that the reduction of frequency in the coating process has had a significant effect on the surface microstructure of the coatings. At low frequencies, the size of pores and protrusions of the coating is increased. It should be noted that by reducing the applied frequency, the amount of spark power increases, and more time is spent in the ignition process, which ultimately leads to larger and deeper pores in the coating surface. Also, at high frequencies, the size of the sparks is smaller, thus reducing the possibility of adsorption of scattered particles in the electrolyte and the pores on the surface are not filled by nanoparticles. But at 1000 Hz, the ignition conditions have improved and it seems that the sparks in the final stage tried to overlap each other, which resulted in a more uniform microstructure.

Fig. 2 (d-f) shows SEM images of the cross-section of coatings from different frequencies. According to the presented images and the thickness values of the coatings in Fig. 3, it is clear that by reducing the frequency of the coating, despite having a large thickness due to very strong

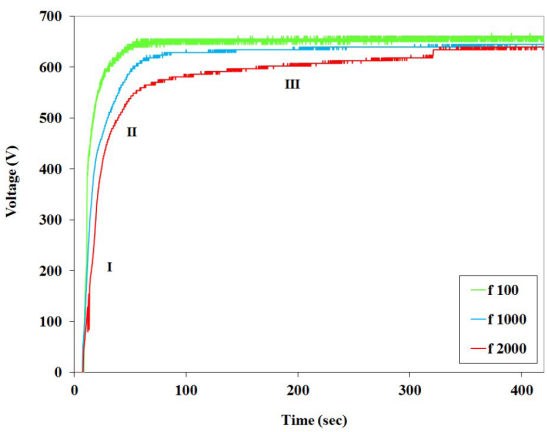

Fig. 1- Voltage-time plots of samples coated at various frequencies in 7 minutes.

sparks, it causes severe non-uniformity with deep holes in the substrate. In fact, by creating stronger sparks, more molten material finds its way to the surface and the coating grows more. But these large sparks damage the coating, which greatly affects the electrochemical properties. In other words, as the energy of the sparks increases, the plasma temperature also rises, resulting in more of the substrate melting in the discharge channels. Higher temperatures also cause more melt to flow. Then, with increasing frequency due to decreasing energy of sparks, growth has decreased.

3.3. Elemental investigation and phase composition of coatings

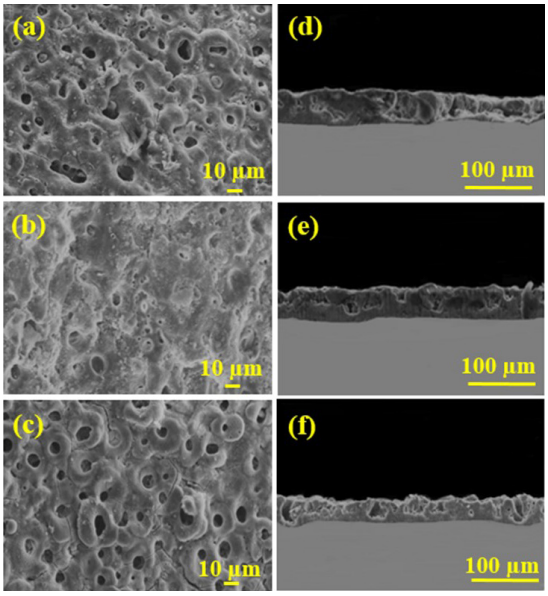

Fig. 2- SEM images from the surface and cross-section of the coatings obtained from the PEO process at various frequencies: (a, d) 100 Hz, (b, e) 1000 Hz, and (c, f) 2000 Hz.

The XRD pattern of the coating created at a frequency of 1000 Hz is shown in Fig. 4. The spectrum of XRD pattern by Grazing method after coating operation indicates the formation of phases in the coating. The composition of the particles in the PEO coating depends on the particle size. Compared to the size of the pores, most of the hydroxyapatite particles are small enough to enter the coating through the drainage channels and be placed in the coating cavities. The peak of hydroxyapatite indicates the neutral entry of nanoparticles into the coating. These nanoparticles entered the coating without changing the chemical composition. The presence of MgO phase peaks indicates that the substrate is melting and oxidizing.

According to reactions 1 to 4, with the onset of the PEO process, first, the dissolution of the Mg alloy occurs (reaction 1), and then the accumulation of oxygen bubbles released from the cathode (reaction 2) occurs in the vicinity of the substrate. Finally, by combining the substrate ions and the electrolyte, a protective oxide coating will be

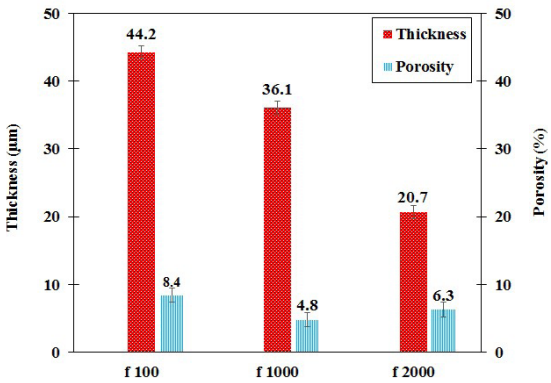

Fig. 3- Thickness and porosity percentage of created coatings at different frequencies.

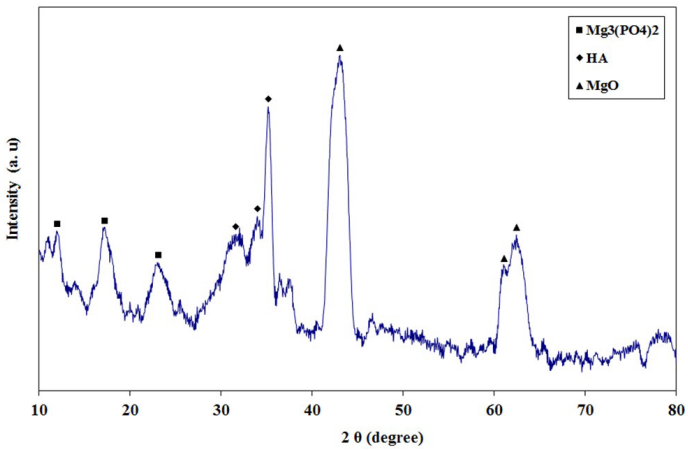

Fig. 4- XRD pattern by grazing method for coating with 1000 Hz.

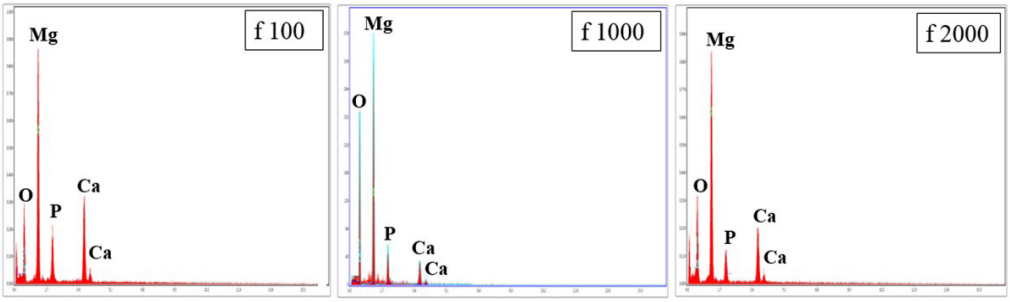

Fig.5- EDS analysis from different coatings.

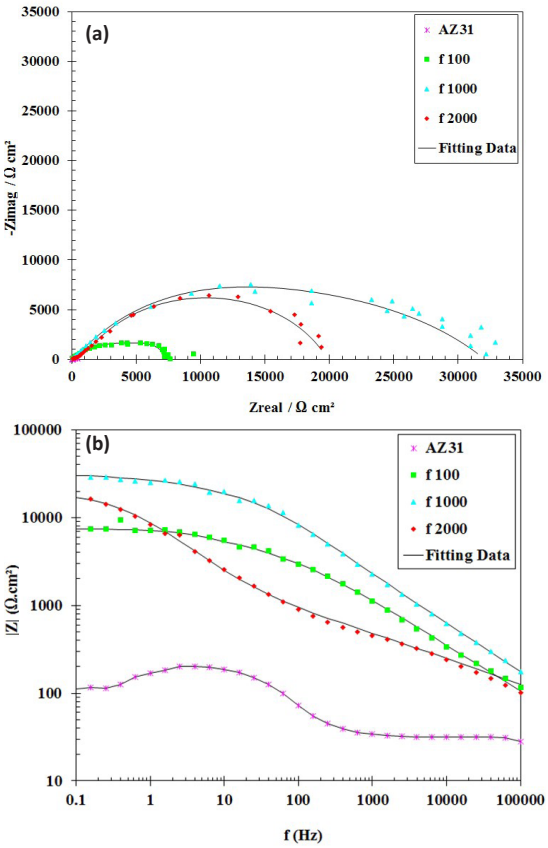

Fig.6- (a) Nyquist and (b) Bode plots of AZ31 alloy and samples coated at various frequencies.

formed according to reaction 4 on the Mg alloy [36].

$$Mg \rightarrow 2Mg^{2+} + 2e^- \quad (1)$$
$$4OH^- \rightarrow H_2O + O_2 + 4e^- \quad (2)$$
$$Mg^{2+} + 4OH^- \rightarrow Mg(OH)_2 \quad (3)$$
$$Mg(OH)_2 \rightarrow MgO + H_2O \quad (4)$$

In addition to the MgO crystal phase, some $Mg_3(PO_4)_2$ phase was also identified in the coating crystal structure. The presence of $Mg_3(PO_4)_2$ phase indicates the reaction between phosphate salt anions and cations resulting from substrate dissolution. Due to the application of a strong electric field between the anode and the cathode, PO_4^{3-} anions in the electrolyte move towards the anode and reacts with Mg^{2+} cations through discharge channels and reaction 5 leads to the formation of $Mg_3(PO_4)_2$ phase in the crystal structure of the coating.

$$Mg^{2+} + PO_4^{3-} \rightarrow Mg_3(PO_4)_2 \quad (5)$$

The results of X-ray energy diffraction spectroscopy from the surface of samples generated at different frequencies are presented in Fig. 5. The main elements of PEO coatings include Ca, P, Mg, and O. As the frequency increases, the elements Ca, P, and O participate in the growth stages of the coating, and their amounts change. As the frequency increases, the presence of O, P, Ca, and Mg decreases. Also, at lower frequencies, due to the longer time of the circuit and consequently the longer the time to adsorption, it is possible to adsorb more nanoparticles in the electrolyte on the surface. Hydroxyapatite particles in the coating electrolyte have zeta-negative potential. These particles migrate to the Mg sample (positive pole) under the influence of a strong electric field between the anode and the cathode. High adsorption of hydroxyapatite particles occurs due to high discharge energy. The particles are placed inside the pores by electrophoretic force. As the frequency decreases, this force increases and causes more nanoparticles to enter the coating.

3.4. Corrosion behavior

3.4.1. EIS tests

Fig. 6 depicts the Bode and Nyquist plots for uncoated samples and coated samples at different frequencies. The Nyquist plot (Fig. 6a) depicts that the uncoated sample has an inductive behavior because a porous oxide layer forms on Mg alloys

when exposed to the atmosphere and when in corrosive solution. Due to the low corrosion performance of this oxide film, the corrosive solution passes through it and reaches the substrate, causing inductive behavior. Nyquist plots have two half-capacitive loops for different specimens. The loop generated at high frequencies corresponds to the outer porous film and at low frequencies to the inner protective layer [66], [67]. Comparing the diameter of the loops in the presented Nyquist diagrams, it can be seen that the f1000 sample has the highest resistance of the inner and outer layer compared to the other two samples. In Bode plots (Fig. 6b) it is observed that at low frequencies the impedance value is higher for a sample with a frequency of 1000 Hz, so increasing the impedance value indicates an increase in corrosion performance.

Table 3- Extracted results from the proposed equivalent circuit

Sample	R_{inner} (kΩ.cm^2)	R_{outer} (kΩ.cm^2)
AZ31B	-	0.42
f 100	1.53	10.3
f 1000	14	36.1
f 2000	2.41	28.7

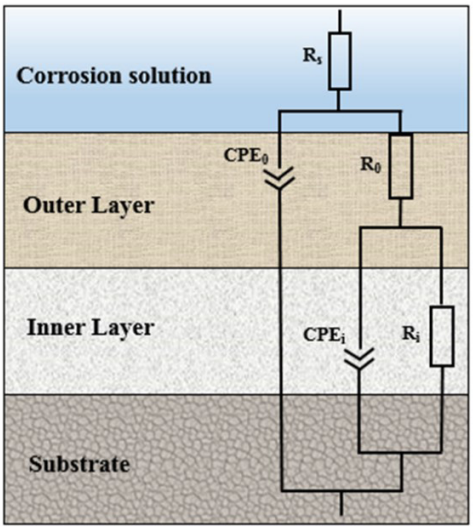

Fig.7- The equivalent circuit for modeling the corrosion behavior of PEO coated samples.

Fig. 7 shows the equivalent circuit [68], [69] for modeling the electrochemical behavior of coatings. A detailed description of this equivalent circuit can be found in a previous publication [55].

The values obtained from modeling the corrosion behavior of coatings are presented in Table 3.

The results show that the coating created at a frequency of 1000 Hz due to the appropriate microstructure has the largest diameter of the Nyquist loop and by nature has the highest corrosion resistance. The coating created at the frequency of 100 Hz has the lowest resistance of the inner layer (1.53 kΩ.cm^2) and the resistance of the outer layer (10.3 kΩ.cm^2) and the coating created at the frequency of 1000 Hz has the highest resistance of the inner layer (14 kΩ.cm^2) and the outer layer resistance (36.1 kΩ.cm^2) and thus the best corrosion behavior.

3.4.2. PDP tests

Fig. 8 shows the PDP curves for coated samples at different frequencies after immersion in SBF solution for 30 minutes. The curve has two branches, cathode and anode, which show changes in corrosion potential in terms of current density.

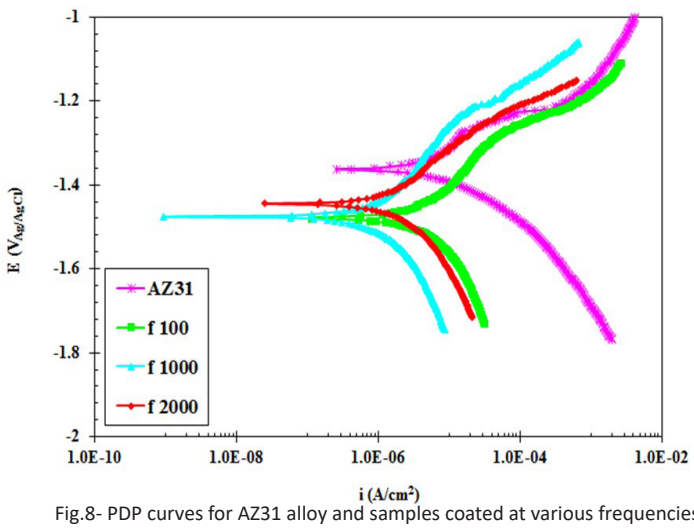

Fig.8- PDP curves for AZ31 alloy and samples coated at various frequencies.

Table 4- Extracted electrochemical results from the PDP plots

Sample	β_a (mV/dec)	β_c (mV/dec)	i_{corr} (A.cm^{-2})	E_{corr} ($V_{Ag/AgCl}$)	R_p (kΩ.cm^2)
AZ31B	41.37	61.21	8.23×10^{-6}	-1.36	12.95
f 100	23.39	11.55	2.17×10^{-7}	-1.49	15.41
f 1000	17.65	26.07	5.83×10^{-8}	-1.45	86.51
f 2000	43.33	33.7	2.06×10^{-7}	-1.47	39.94

The corrosion current density was obtained using the Tafel extrapolation method, which can be used to accurately measure polarization resistance.

By applying ceramic coatings to AZ31B alloy, the PDP curves of all coatings are shifted towards a more negative potential and lower corrosion current density than the substrate. This shows that the application of ceramic coating increased the thermodynamic tendency for corrosion to occur, while the corrosion kinetics decreased. Polarization resistance can be calculated using the Stern-Geary equation [70]:

$$R_p = \frac{\beta_a \beta_c}{2.3(\beta_a+\beta_c)i_{corr}} \quad (6)$$

Porosity, which is one of the most important defects of coatings created by the PEO method, plays an important role in various properties of the coating, especially in its corrosion resistance, because the corrosive liquid through these porosities can penetrate into the coating and eventually destroy the coating to reach the substrate. Equation 7 shows the relationship between the porosity of the coating (P) and the electrochemical parameters resulting from the PDP plots.

$$p = \left(\frac{Rps}{Rp}\right) \times 10^{-\left(\frac{\Delta Ecorr}{\beta a}\right)} \times 100 \quad (7)$$

In equation 7, R_{ps} and R_p show the corrosion resistance of the substrate and the coating, and ΔE_{corr} shows the corrosion potential difference between the substrate and the coating [70], [71]. Electrochemical data extracted from Fig. 8 and porosity percentage are presented in Table 4. There was a good correlation between the percentage of porosity obtained from SEM images and the percentage of porosity obtained from Equation 7. All three coated specimens had higher corrosion resistance than the uncoated specimen. This indicates that the PEO process significantly increased the corrosion performance of the substrate. By comparing the corrosion resistance of coatings and the percentage of porosity reported in Table 4, it can be seen that there is a relationship between these two parameters. The coated sample at the frequency of 1000 Hz has the lowest percentage of porosity (14%) and the lowest corrosion current density (5.83×10^{-8} A/cm^2) and as a result has the highest polarization resistance (86.51 kΩ.cm^2).

4. Conclusion

In this study, the influence of coating frequency (100, 1000, and 2000 Hz) on corrosion behavior and microstructure of oxide coatings created on AZ31B Mg substrate was investigated. SEM images showed that the best results were obtained in the coating created at a frequency of 1000 Hz. The coating obtained from these conditions had the densest structure with cavities with the lowest average size (4.8%). The result of the XRD pattern showed that the major phase of the coating was MgO, hydroxyapatite, and $Mg_3(PO_4)_2$, which is due to the reaction between the anion and cation within the electrolyte. EIS and PDP measurements showed that the PEO process effectively improves the corrosion behavior of AZ31B alloy. Also, the coating created at a frequency of 1000 Hz had the lowest corrosion current density (5.83×10^{-8} A/cm^2).

References

1. Gray JE, Luan B. Protective coatings on magnesium and its alloys — a critical review. Journal of Alloys and Compounds. 2002;336(1-2):88-113.
2. Zhang Y, Yan C. Development of anodic film on Mg alloy AZ91D. Surface and Coatings Technology. 2006;201(6):2381-6.
3. James DW. High damping metals for engineering applications. Materials Science and Engineering. 1969;4(1):1-8.
4. Keyvani A, Zamani M, Fattah-Alhosseini A, Nourbakhsh SH, Bahamirian M. Microstructure and corrosion resistance of MAO coatings on AZ31 magnesium. Materials Research Express. 2018;5(8):086510.
5. Das AK. Recent trends in laser cladding and alloying on magnesium alloys: A review. Materials Today: Proceedings. 2021;51:723-7.
6. Yang Y, Xiong X, Chen J, Peng X, Chen D, Pan F. Research advances in magnesium and magnesium alloys worldwide in 2020. Journal of Magnesium and Alloys. 2021.
7. Prasad SVS, Prasad SB, Verma K, Mishra RK, Kumar V, Singh S. The role and significance of Magnesium in modern day research-A review. Journal of Magnesium and Alloys. 2021;10(1):1-61.

8. Chaharmahali R, Fattah-alhosseini A, Babaei K. Surface characterization and corrosion behavior of calcium phosphate (Ca-P) base composite layer on Mg and its alloys using plasma electrolytic oxidation (PEO): A review. Journal of Magnesium and Alloys. 2021;9(1):21-40.
9. Sezer N, Evis Z, Kayhan SM, Tahmasebifar A, Koç M. Review of magnesium-based biomaterials and their applications. Journal of Magnesium and Alloys. 2018;6(1):23-43.
10. Chaharmahali R, Fattah-alhosseini A, Nouri M, Babaei K. Improving surface characteristics of PEO coatings of Mg and its alloys with zirconia nanoparticles: a review. Applied Surface Science Advances. 2021;6:100131.
11. Fattah-alhosseini A, Sabaghi Joni M. Effect of KOH Concentration on the Microstructure and Electrochemical Properties of MAO-Coated Mg Alloy AZ31B. Journal of Materials Engineering and Performance. 2015;24(9):3444-52.
12. Liang J, Hu L, Hao J. Characterization of microarc oxidation coatings formed on AM60B magnesium alloy in silicate and phosphate electrolytes. Applied Surface Science. 2007;253(10):4490-6.
13. Zhang Z-Q, Wang L, Zeng M-Q, Zeng R-C, Kannan MB, Lin C-G, et al. Biodegradation behavior of micro-arc oxidation coating on magnesium alloy-from a protein perspective. Bioact Mater. 2020;5(2):398-409.
14. Sekar P, S N, Desai V. Recent progress in in vivo studies and clinical applications of magnesium based biodegradable implants – A review. Journal of Magnesium and Alloys. 2021.
15. Zhang D, Peng F, Liu X. Protection of magnesium alloys: From physical barrier coating to smart self-healing coating. Journal of Alloys and Compounds. 2020;853:157010.
16. Fattah-alhosseini A, Joni MS. Role of chloride in the electrochemical behaviour of AZ31B Mg alloy. International Journal of Materials Research. 2015;106(3):282-7.
17. Harada Y, Kumai S. Effect of ceramics coating using sol–gel processing on corrosion resistance and age hardening of AZ80 magnesium alloy substrate. Surface and Coatings Technology. 2013;228:59-67.
18. Kuo Y-L, Chang K-H. Atmospheric pressure plasma enhanced chemical vapor deposition of SiOx films for improved corrosion resistant properties of AZ31 magnesium alloys. Surface and Coatings Technology. 2015;283:194-200.
19. Tang H, Gao Y. Preparation and characterization of hydroxyapatite containing coating on AZ31 magnesium alloy by micro-arc oxidation. Journal of Alloys and Compounds. 2016;688:699-708.
20. Gu XN, Li N, Zhou WR, Zheng YF, Zhao X, Cai QZ, et al. Corrosion resistance and surface biocompatibility of a microarc oxidation coating on a Mg–Ca alloy. Acta Biomaterialia. 2010;7(4):1880-9.
21. Fattah-Alhosseini A, Vakili-Azghandi M, Keshavarz MK. Influence of Concentrations of KOH and Na2SiO3 Electrolytes on the Electrochemical Behavior of Ceramic Coatings on 6061 Al Alloy Processed by Plasma Electrolytic Oxidation. Acta Metallurgica Sinica (English Letters). 2016;29(3):274-81.
22. Fattah-alhosseini A, Chaharmahali R, Babaei K. Effect of particles addition to solution of plasma electrolytic oxidation (PEO) on the properties of PEO coatings formed on magnesium and its alloys: A review. Journal of Magnesium and Alloys. 2020;8(3):799-818.
23. Wang X, Yan H, Hang R, Shi H, Wang L, Ma J, et al. Enhanced anticorrosive and antibacterial performances of silver nanoparticles/polyethyleneimine/MAO composite coating on magnesium alloys. Journal of Materials Research and Technology. 2021;11:2354-64.
24. Yang S, Sun R, Chen K. Self-healing performance and corrosion resistance of phytic acid/cerium composite coating on microarc-oxidized magnesium alloy. Chemical Engineering Journal. 2022;428:131198.
25. Yeganeh M, Mohammadi N. Superhydrophobic surface of Mg alloys: A review. Journal of Magnesium and Alloys. 2018;6(1):59-70.
26. Babaei K, Fattah-alhosseini A, Chaharmahali R. A review on plasma electrolytic oxidation (PEO) of niobium: Mechanism, properties and applications. Surfaces and Interfaces. 2020;21:100719.
27. Lin Z, Wang T, Yu X, Sun X, Yang H. Functionalization treatment of micro-arc oxidation coatings on magnesium alloys: a review. Journal of Alloys and Compounds. 2021;879:160453.
28. Toorani M, Aliofkhazraei M. Review of electrochemical properties of hybrid coating systems on Mg with plasma electrolytic oxidation process as pretreatment. Surfaces and Interfaces. 2019;14:262-95.
29. Attarzadeh N, Ramana CV. Plasma Electrolytic Oxidation Ceramic Coatings on Zirconium (Zr) and ZrAlloys: Part I—Growth Mechanisms, Microstructure, and Chemical Composition. Coatings. 2021;11(6):634.
30. Nikoomanzari E, Fattah-alhosseini A, Pajohi Alamoti MR, Keshavarz MK. Effect of ZrO2 nanoparticles addition to PEO coatings on Ti–6Al–4V substrate: Microstructural analysis, corrosion behavior and antibacterial effect of coatings in Hank's physiological solution. Ceramics International. 2020;46(9):13114-24.
31. Roknian M, Fattah-alhosseini A, Gashti SO. Plasma Electrolytic Oxidation Coatings on Pure Ti Substrate: Effects of Na3PO4 Concentration on Morphology and Corrosion Behavior of Coatings in Ringer's Physiological Solution. Journal of Materials Engineering and Performance. 2018;27(3):1343-51.
32. Molaei M, Fattah-Alhosseini A, Gashti SO. Sodium Aluminate Concentration Effects on Microstructure and Corrosion Behavior of the Plasma Electrolytic Oxidation Coatings on Pure Titanium. Metallurgical and Materials Transactions A. 2017;49(1):368-75.
33. Rahman M, Li Y, Wen C. HA coating on Mg alloys for biomedical applications: A review. Journal of Magnesium and Alloys. 2020;8(3):929-43.
34. Fattah-alhosseini A, Chaharmahali R. Enhancing corrosion and wear performance of PEO coatings on Mg alloys using graphene and graphene oxide additions: A review. FlatChem. 2021;27:100241.
35. Wen C, Zhan X, Huang X, Xu F, Luo L, Xia C. Characterization and corrosion properties of hydroxyapatite/graphene oxide bio-composite coating on magnesium alloy by one-step micro-arc oxidation method. Surface and Coatings Technology. 2017;317:125-33.
36. Barati Darband G, Aliofkhazraei M, Hamghalam P, Valizade N. Plasma electrolytic oxidation of magnesium and its alloys: Mechanism, properties and applications. Journal of Magnesium and Alloys. 2017;5(1):74-132.
37. Babaei K, Fattah-alhosseini A, Molaei M. The effects of carbon-based additives on corrosion and wear properties of Plasma electrolytic oxidation (PEO) coatings applied on Aluminum and its alloys: A review. Surfaces and Interfaces. 2020;21:100677.
38. Li C-Y, Fan X-L, Cui L-Y, Zeng R-C. Corrosion resistance and electrical conductivity of a nano ATO-doped MAO/methyltrimethoxysilane composite coating on magnesium alloy AZ31. Corrosion Science. 2020;168:108570.
39. Attarzadeh N, Ramana CV. Plasma Electrolytic Oxidation Ceramic Coatings on Zirconium (Zr) and Zr-Alloys: Part-II: Properties and Applications. Coatings. 2021;11(6):620.

40. Clyne TW, Troughton SC. A review of recent work on discharge characteristics during plasma electrolytic oxidation of various metals. International Materials Reviews. 2018;64(3):127-62.
41. Mohedano M, Lu X, Matykina E, Blawert C, Arrabal R, Zheludkevich ML. Plasma Electrolytic Oxidation (PEO) of Metals and Alloys. Encyclopedia of Interfacial Chemistry: Elsevier; 2018. p. 423-38.
42. Asgari M, Aliofkhazraei M, Barati Darband G, Sabour Rouhaghdam A. How nanoparticles and submicron particles adsorb inside coating during plasma electrolytic oxidation of magnesium? Surface and Coatings Technology. 2020;383:125252.
43. Rafieerad AR, Ashra MR, Mahmoodian R, Bushroa AR. Surface characterization and corrosion behavior of calcium phosphate-base composite layer on titanium and its alloys via plasma electrolytic oxidation: A review paper. Materials Science and Engineering: C. 2015;57:397-413.
44. Monetta T, Parnian P, Acquesta A. Recent Advances in the Control of the Degradation Rate of PEO Treated Magnesium and Its Alloys for Biomedical Applications. Metals. 2020;10(7):907.
45. Shi L, Xu Y, Li K, Yao Z, Wu S. Effect of additives on structure and corrosion resistance of ceramic coatings on Mg–Li alloy by micro-arc oxidation. Current Applied Physics. 2010;10(3):719-23.
46. Tang Y, Zhao X, Jiang K, Chen J, Zuo Y. The influences of duty cycle on the bonding strength of AZ31B magnesium alloy by microarc oxidation treatment. Surface and Coatings Technology. 2010;205(6):1789-92.
47. Bala Srinivasan P, Liang J, Balajeee RG, Blawert C, Störmer M, Dietzel W. Effect of pulse frequency on the microstructure, phase composition and corrosion performance of a phosphate-based plasma electrolytic oxidation coated AM50 magnesium alloy. Applied Surface Science. 2010;256(12):3928-35.
48. Shang W, Wu F, Wang Y, Rabiei Baboukani A, Wen Y, Jiang J. Corrosion Resistance of Micro-Arc Oxidation/Graphene Oxide Composite Coatings on Magnesium Alloys. ACS Omega. 2020;5(13):7262-70.
49. Asgari M, Aliofkhazraei M, Darband GB, Rouhaghdam AS. Evaluation of alumina nanoparticles concentration and stirring rate on wear and corrosion behavior of nanocomposite PEO coating on AZ31 magnesium alloy. Surface and Coatings Technology. 2017;309:124-35.
50. Wang Z, Ma Y, Wang Y. Effect of V2O5 Additive on Micro-Arc Oxidation Coatings Fabricated on Magnesium Alloys with Different Loading Voltages. Metals. 2020;10(9):1146.
51. Lu X, Blawert C, Mohedano M, Scharnagl N, Zheludkevich ML, Kainer KU. Influence of electrical parameters on particle uptake during plasma electrolytic oxidation processing of AM50 Mg alloy. Surface and Coatings Technology. 2016;289:179-85.
52. Zhang L, Zhang J, Chen C-f, Gu Y. Advances in microarc oxidation coated AZ31 Mg alloys for biomedical applications. Corrosion Science. 2015;91:7-28.
53. Sankara Narayanan TSN, Park IS, Lee MH. Strategies to improve the corrosion resistance of microarc oxidation (MAO) coated magnesium alloys for degradable implants: Prospects and challenges. Progress in Materials Science. 2014;60:1-71.
54. Hafili F, Chaharmahali R, Babaei K, Fattah-alhosseini A. Duty cycle influence on the corrosion behavior of coatings created by plasma electrolytic oxidation on AZ31B magnesium alloy in simulated body fluid. Corrosion Communications. 2021;3:62-70.
55. Chaharmahali R, Fattah-Alhosseini A, Esfahani H. Increasing the in-vitro corrosion resistance of AZ31B-Mg alloy via coating with hydroxyapatite using plasma electrolytic oxidation. Journal of Asian Ceramic Societies. 2020;8(1):39-49.
56. Mohedano M, Lu X, Matykina E, Blawert C, Arrabal R, Zheludkevich ML. Plasma Electrolytic Oxidation (PEO) of Metals and Alloys. Encyclopedia of Interfacial Chemistry: Elsevier; 2018. p. 423-38.
57. Duan H, Yan C, Wang F. Effect of electrolyte additives on performance of plasma electrolytic oxidation films formed on magnesium alloy AZ91D. Electrochimica Acta. 2007;52(11):3785-93.
58. Lee S-J, Do LHT. Effects of copper additive on micro-arc oxidation coating of LZ91 magnesium-lithium alloy. Surface and Coatings Technology. 2016;307:781-9.
59. NasiriVatan H, Ebrahimi-Kahrizsangi R, Asgarani MK. Tribological performance of PEO-WC nanocomposite coating on Mg Alloys deposited by Plasma Electrolytic Oxidation. Tribology International. 2016;98:253-60.
60. Toorani M, Aliofkhazraei M, Sabour Rouhaghdam A. Microstructural, protective, inhibitory and semiconducting properties of PEO coatings containing CeO2 nanoparticles formed on AZ31 Mg alloy. Surface and Coatings Technology. 2018;352:561-80.
61. Guo HF, An MZ, Huo HB, Xu S, Wu LJ. Microstructure characteristic of ceramic coatings fabricated on magnesium alloys by micro-arc oxidation in alkaline silicate solutions. Applied Surface Science. 2006;252(22):7911-6.
62. Wang YM, Wang FH, Xu MJ, Zhao B, Guo LX, Ouyang JH. Microstructure and corrosion behavior of coated AZ91 alloy by microarc oxidation for biomedical application. Applied Surface Science. 2009;255(22):9124-31.
63. Liu F, Shan D-y, Song Y-w, Han E-h. Formation process of composite plasma electrolytic oxidation coating containing zirconium oxides on AM50 magnesium alloy. Transactions of Nonferrous Metals Society of China. 2011;21(4):943-8.
64. Toorani M, Aliofkhazraei M, Golabadi M, Rouhaghdam AS. Effect of lanthanum nitrate on the microstructure and electrochemical behavior of PEO coatings on AZ31 Mg alloy. Journal of Alloys and Compounds. 2017;719:242-55.
65. Zhu J, Jia H, Liao K, Li X. Improvement on corrosion resistance of micro-arc oxidized AZ91D magnesium alloy by a pore-sealing coating. Journal of Alloys and Compounds. 2021;889:161460.
66. Ko YG, Lee KM, Shin DH. Electrochemical Corrosion Properties of AZ91 Mg Alloy via Plasma Electrolytic Oxidation and Subsequent Annealing. MATERIALS TRANSACTIONS. 2011;52(8):1697-700.
67. Yang J, Lu X, Blawert C, Di S, Zheludkevich ML. Microstructure and corrosion behavior of Ca/P coatings prepared on magnesium by plasma electrolytic oxidation. Surface and Coatings Technology. 2017;319:359-69.
68. Tang H, Wu T, Wang H, Jian X, Wu Y. Corrosion behavior of HA containing ceramic coated magnesium alloy in Hank's solution. Journal of Alloys and Compounds. 2017;698:643-53.
69. Mann R, Grman V, Hansal WEG. Optimisation of PEO layers with incorporated nanoparticles. Transactions of the IMF. 2021;99(1):10-6.
70. Stern M. Closure to "Discussion of 'Electrochemical Polarization, 1. A Theoretical Analysis of the Shape of Polarization Curves' [M. Stern and A. L. Geary (pp. 56–63, Vol. 104)]". Journal of The Electrochemical Society. 1957;104(12):751.
71. Madhan Kumar A, Kwon SH, Jung HC, Shin KS. Corrosion protection performance of single and dual Plasma Electrolytic Oxidation (PEO) coating for aerospace applications. Materials Chemistry and Physics. 2015;149-150:480-6.